Z-99 WAVE-EQUATION MIGRATION VELOCITY ANALYSIS

PAUL SAVA AND BIONDO BIONDI
Geophysics Department, Stanford University, Stanford, CA 94305, USA

1 Summary

We overcome the limitations of conventional MVA in regions of high wavefield complexity (subsalt) using a wave-equation migration velocity analysis technique (Sava and Biondi, 2004a,a), and illustrate it on a realistic synthetic salt-dome dataset. We model subsalt propagation by implicitly using wavepaths created using one-way wavefield extrapolation. Those wavepaths are much more accurate and robust than broadband rays, since they inherit the frequency dependence and multipathing of the underlying wavefield. We formulate the objective function for our optimization in the image space by relating an image perturbation to a perturbation of the velocity model. The image perturbations are defined using linearized prestack residual migration, thus ensuring stability relative to the first-order Born approximation assumptions. Numeric examples demonstrate that wave-equation MVA is an effective tool for subsalt velocity analysis, even when shadows and illumination gaps are present.

2 Introduction

Depth imaging of complex structures depends on the quality of the velocity model. However, conventional Migration Velocity Analysis (MVA) procedures often fail when the wavefield is severely distorted by lateral velocity variations and thus complex multipathing occurs. Imaging under rugged salt bodies is an important case when ray-based MVA methods are not reliable. Wave-equation MVA (Biondi and Sava, 1999; Sava and Fomel, 2002; Sava and Biondi, 2004a,b) is based on wavefield continuation methods and has the potential of overcoming these limitations of ray-based MVA methods. In this paper, we present an application of WEMVA to Sigsbee 2A, a realistic and challenging 2-D synthetic data set created by the SMAART JV (Paffenholz et al., 2002).

A practical difficulty encountered when using rays to estimate velocity below salt bodies with rough boundaries is the instability of ray tracing. Rough salt topographies create poorly illuminated areas, or even shadow zones, in the subsalt region. The spatial distributions of these poorly illuminated areas is very sensitive to the velocity function. Therefore, it is often extremely difficult to trace the rays that connect a given point in the poorly illuminated areas with a given point at the surface (two-point ray-

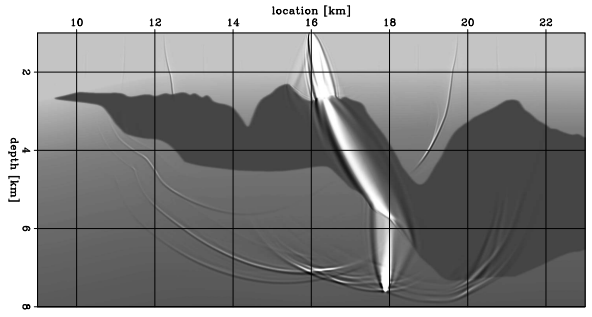


Figure 1: Wavepaths illustrating the complexity of wave propagation through rough salt bodies.

tracing). Furthermore, rays are a poor approximations of the actual wavepaths when a band-limited seismic wave propagates through a rugose top of the salt. Wavefield-extrapolation methods are robust with respect to shadow zones and provide wavepaths usable for velocity inversion (Figure 1).

The limited and uneven "illumination" of both the reflectivity model and the velocity model in the subsalt region is a challenging problem for both WEMVA and conventional ray-based MVA. The angular range drastically shrinks in Angle Domain Common Image Gathers (ADCIGs) for subsalt reflectors. This phenomenon is caused by a lack of oblique wavepaths in the subsalt and deteriorates the "sampling" of the velocity variations.

3 Example of WEMVA applied to a subsalt data set

For our example, we concentrate on the lower part of the model, simulate a common subsalt velocity analysis situation when the shape of the salt is known, but the smoothly varying slowness subsalt is not known. Figure 2 highlights several characteristics of this model which make it challenging for migration velocity analysis. Most of them are related to the complicated wavepaths in the subsurface under rough salt bodies. Firstly, the angular coverage under salt ($x > 11$ km) is much smaller than in the sedimentary section uncovered by salt ($x < 11$ km). Secondly, the subsalt region is marked by many illumination gaps or shadow zones, the most striking being located at $x = 12$ and $x = 19$ km. Velocity analysis in such areas is less constrained than in the well illuminated zones.

We first migrating the data with the background slowness (Figure 2). The top panel depicts the zero offset of the prestack migrated image, and the bottom panel depicts ADCIGs at equally spaced locations in the image. Since the migration velocity is incorrect, the image is less well focused and the angle gathers show significant moveout. Furthermore, the diffractors at depths $z = 7.5$ km, and the fault at $x = 15$ km are defocused.

As described in Sava and Biondi (2004a,b), we run prestack Stolt residual migration for various values of the velocity ratio parameter ρ between 0.9 and 1.6, which ensures that we span a fairly wide range of the velocity space. Although residual migration operates on the entire image at once, for display purposes we extract one gather at $x = 10$ km. Figure 3 shows at the top the ADCIGs for all velocity ratios and at the bottom the semblance panels computed from the ADCIGs. We pick the maximum semblance at all locations and all depths together with an estimate of the reliability of every picked value which we use as a weighting function on the data residuals during inversion.

Based on the picked velocity ratio, we compute linearized differential image perturbations and invert for the slowness perturbation (Sava and Biondi, 2004a,b). Finally, we update the slowness model and remigrate the data (Figure 4). The reflectors are pushed back to their correct positions, the diffractors at $z = 7.5$ km are focused and the ADCIGs are flatter than in the background image, indicating improved

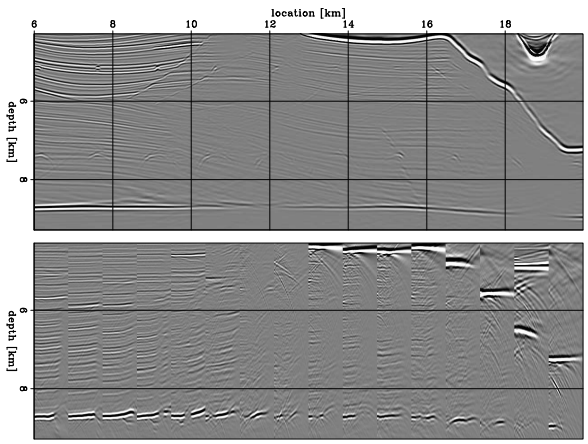


Figure 2: Migration with the background slowness. The zero offset of the prestack migrated image (top) and angle-domain common image gathers at equally spaced locations in the image (bottom). Each ADCIG corresponds roughly to the location right above it.

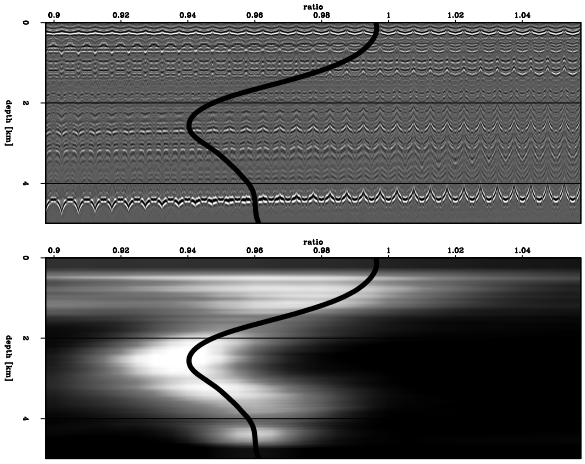


Figure 3: Residual migration for a CIG at $x = 10$ km. The top panel depicts angle-domain common-image gathers for all values of the velocity ratio, and the bottom panel depicts semblance panels used for picking. All gathers are stretched to eliminate the vertical movement corresponding to different migration velocities. The overlain line indicates the picked values at all depths.

image quality.

Figures 5-6 show a more detailed analysis of the results of our inversion displayed as ADCIGs at various locations in the image. In each figure, the panels correspond to migration with the correct slowness (left), the background slowness (center), and the updated slowness (right). Figure 5 corresponds to an ADCIG at $x = 10$ km, in the region with illumination gaps, which are clearly visible on the strong reflector at $z = 9$ km at a scattering angle of about 20°. The gaps are preserved in the ADCIG from the image migrated with the background slowness, but the moveouts are still easy to identify and correct. Figure 6 corresponds to an ADCIG at $x = 12$ km, in a region which is hardly illuminated at all. Thus, this ADCIG is much noisier and the moveouts are harder to identify and measure, yet we can still recover an image which is reasonably similar to the one obtained by migration with the correct slowness.

A simple visual comparison of the middle panels with the right and left panels in Figures 5-6 unequivocally demonstrates that our WEMVA method overcomes the limitations related to the linearization of the wave equation by using the first-order Born approximation. The images obtained using the initial velocity model (middle panels) are vertically shifted by several wavelengths with respect to the images obtained using the true velocity (left panels) and the estimated velocity (right panels).

4 Conclusions

We demonstrate that Wave-Equation Migration Velocity Analysis (WEMVA) overcomes many of the problems encountered by ray-based MVA methods when estimating velocity under salt. We illus-

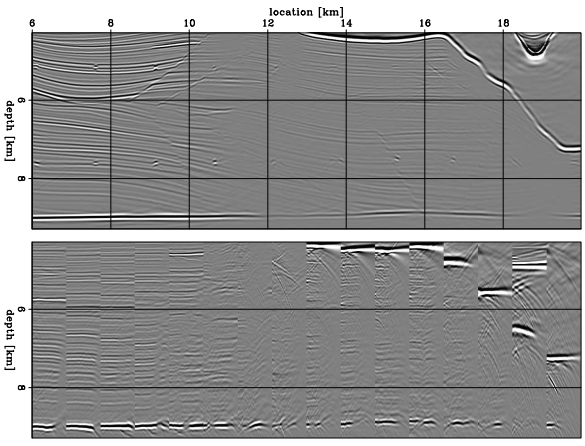


Figure 4: Migration with the updated slowness. The zero offset of the prestack migrated image (top) and angle-domain common image gathers at equally spaced locations in the image (bottom). Each ADCIG corresponds roughly to the location right above it.

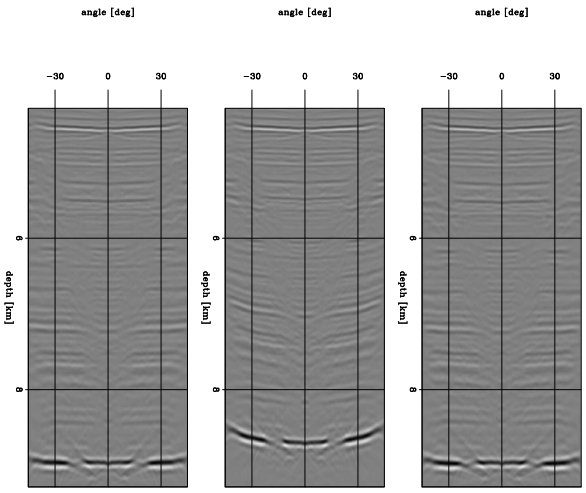


Figure 5: Angle-domain common-image gathers at $x = 10$ km. Each panel corresponds to a different migration velocity: migration with the correct velocity (left), migration with the background velocity (center) and migration with the updated velocity (right).

trate with numerical examples that wavepaths computed by wavefield extrapolation are robust with respect to shadow zones, and they model the finite-frequency wave propagation that occurs in such environments better than rays do. We demonstrate that velocity errors can be effectively measured by residual migration scans. These scans provide useful velocity information almost in all the subsalt areas, though the reliability of these measurements decreases where poor illumination drastically deteriorates the quality of ADCIGs.

5 REFERENCES

Biondi, B., and Sava, P., 1999, Wave-equation migration velocity analysis *in* 69th Ann. Internat. Mtg. Soc. of Expl. Geophys., 1723–1726.

Paffenholz, J., McLain, B., Zaske, J., and Keliher, P., 2002, Subsalt multiple attenuation and imaging: Observations from the Sigsbee2B synthetic dataset *in* 72nd Ann. Internat. Mtg. Soc. of Expl. Geophys., 2122–2125.

Sava, P., and Biondi, B., 2004a, Wave-equation migration velocity analysis—I: Theory: Geophysical Prospecting, submitted for publication.

—, 2004b, Wave-equation migration velocity analysis—II: Examples: Geophysical Prospecting, submitted for publication.

Sava, P., and Fomel, S., 2002, Wave-equation migration velocity analysis beyond the Born approximation *in* 72nd Ann. Internat. Mtg. Soc. of Expl. Geophys., 2285–2288.

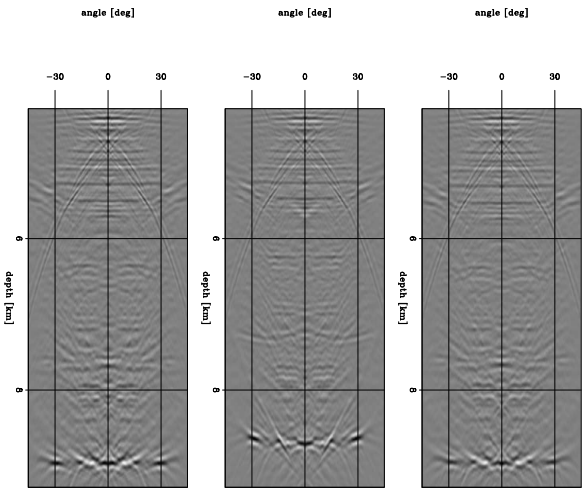


Figure 6: Angle-domain common-image gathers at $x = 12$ km. Each panel corresponds to a different migration velocity: migration with the correct velocity (left), migration with the background velocity (center) and migration with the updated velocity (right).